Spatiotemporally tracking of nano-biofilaments inside the nuclear pore complex core

Biomaterials 256 (2020) 120198

Contents lists available at ScienceDirect

Biomaterials

journal homepage: www.elsevier.com/locate/biomaterials

Spatiotemporally tracking of nano-biofilaments inside the nuclear pore complex core

Mahmoud Shaaban Mohamed[a,b], Masaharu Hazawa[a], Akiko Kobayashi[a], Laurent Guillaud[c], Takahiro Watanabe-Nakayama[d], Mizuho Nakayama[d,e], Hanbo Wang[a], Noriyuki Kodera[d], Masanobu Oshima[d,e], Toshio Ando[d], Richard W. Wong[a,d,*]

[a] Cell-Bionomics Research Unit, Innovative Integrated Bio-Research Core, Institute for Frontier Science Initiative, Kanazawa University, Kanazawa, 920-1192, Japan
[b] Zoology Department, Faculty of Science, Assiut University, Assiut, 71516, Egypt
[c] Molecular Neuroscience Unit, Okinawa Institute of Science and Technology Graduate University, Okinawa, 904-0495, Japan
[d] WPI Nano Life Science Institute (WPI-NanoLSI), Kanazawa University, Kanazawa, 920-1192, Japan
[e] Division of Genetics, Cancer Research Institute, Kanazawa University, Kanazawa, Japan

ARTICLE INFO

Keywords:
NPC
LLPS
HS-AFM
Nanopore
Colon cancer
Organoid
IDR

ABSTRACT

Nuclear pore complex (NPC) is a gating nanomachine with a central selective barrier composed mainly of Nups, which contain intrinsically disordered (non-structured) regions (IDRs) with phenylalanine-glycine (FG) motifs (FG-NUPs). The NPC central FG network dynamics is poorly understood, as FG-NUPs liquid-liquid phase separation (LLPS) have evaded structural characterization. Moreover, the working mechanism of single FG-NUP-biofilaments residing at the central lumen is unknown. In general, flexible biofilaments are expected to be tangled and knotted during their motion and interaction. However, filament knotting visualization in real-time and space has yet to be visualized at the nanoscale. Here, we report a spatiotemporally tracking method for FG-NUP organization with nanoscale resolution, unveiling FG-NUP conformation in NPCs of colorectal cells and organoids at timescales of ~150 ms using high-speed atomic force microscopy (HS-AFM). Tracking of FG-NUP single filaments revealed that single filaments have a heterogeneous thickness in normal and cancer models which in turn affected the filament rotation and motion. Notably, FG-NUPs are overexpressed in various cancers. Using the FG-NUP inhibitor, *trans*-1,2-cyclohexanediol, we found that central plug size was significantly reduced and incompletely reversible back to filamentous structures in aggressive colon cancer cells and organoids. These data showed a model of FG-NUPs reversible self-assembly devolving into the central plug partial biogenesis. Taken together, HS-AFM enabled the tracking and manipulation of single filaments of native FG-NUPs which has remained evasive for decades.

1. Introduction

The nuclear pore complex (NPC) is a biomolecular "nanogate-keeper" that controls nucleocytoplasmic transport in eukaryotic cells [1–4]. The central component of the functional architecture of the NPC is the assembly of nucleoporins containing repeats of phenylalanine glycine (FG), known as FG-NUPs. The FG-NUPs are a class of intrinsically disordered proteins (IDPs) that contain intrinsically disordered regions (IDRs) and lack well-defined tertiary structures. FG-NUPs also go through liquid–liquid phase separation (LLPS) and form liquid-like protein droplets that mimic permeability barrier properties of NPCs [5]. Much of our knowledge of the properties of FG-NUPs is derived from *in vitro* experiments augmented by theoretical and computational modeling. A number of hypotheses have been put forward to answer these questions [6]. The models have made tremendous inroads into our understanding of how FG-NUPs optimizing as a nanoscale selective barrier, but a clear spatiotemporal physical understanding of the FG-NUP dynamic IDR structure is still missing. Moreover, how NPCs can form a central plug (CP) and maintain fast, efficient and selective bidirectional transport in highly crowded conditions has been unclear

Abbreviations: list: CP, central plug; CRC, colorectal cancer; DIF-1, differentiation-inducing factor-1; FG, phenylalanine glycine; HS-AFM, High-Speed Atomic Force Microscopy; IDP, intrinsically disordered proteins; IDR, intrinsically disordered domains; LLPS, liquid–liquid phase separation; NPC, nuclear pore complex; PLL, poly-L-lysine

* Corresponding author. WPI Nano Life Science Institute (WPI-NanoLSI), Kanazawa University, Kanazawa, 920-1192, Japan.
E-mail address: rwong@staff.kanazawa-u.ac.jp (R.W. Wong).

https://doi.org/10.1016/j.biomaterials.2020.120198
Received 13 December 2019; Received in revised form 7 April 2020; Accepted 9 June 2020
Available online 23 June 2020

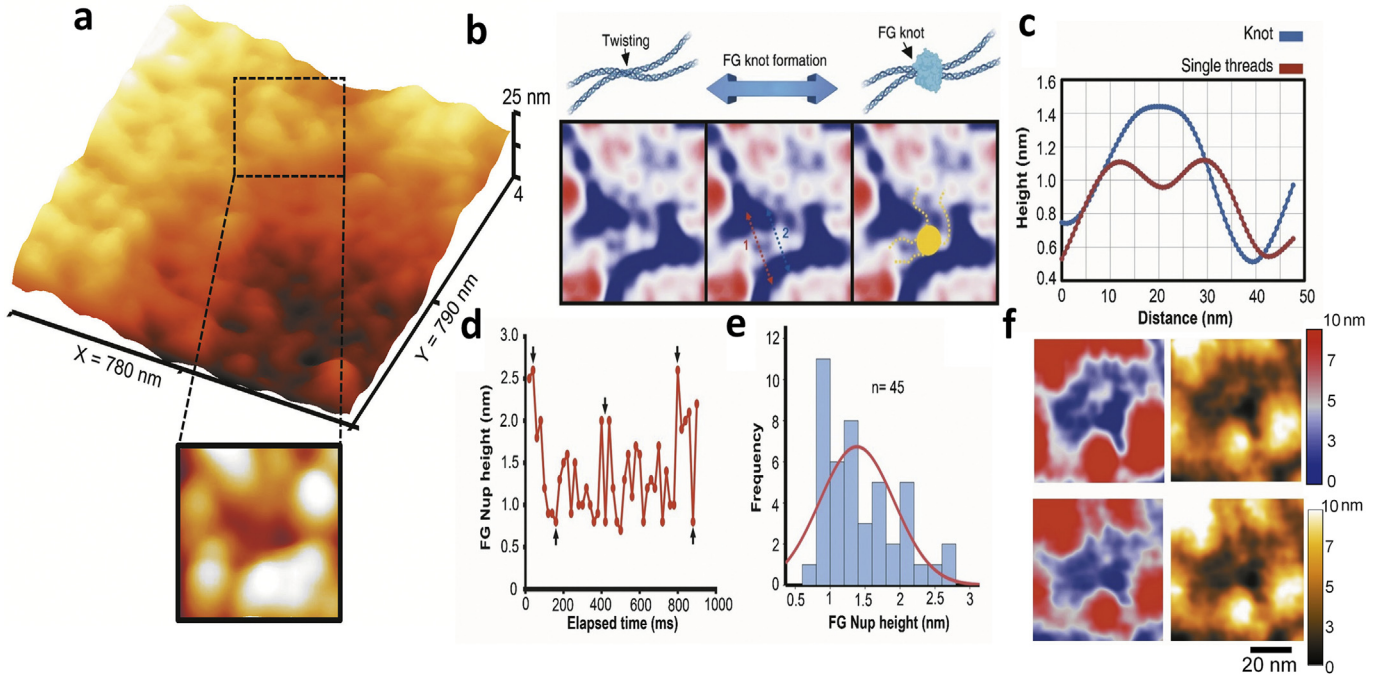

Fig. 1. Transient rapid conformations of FG-NUP complexes inside the native NPCs. (a) HS-AFM image of the native cytoplasmic face of nuclear envelope of HCT116 cells is shown in 3D format with enlarged view of a single pore as scanning illustration. The single NPC is tracked to determine the dynamic conformations at a high nanometer resolution. Z-range is 25 nm, scanning speed is 2 frames per second, 200 × 200 pixels **(b)** HS-AFM images showing two single FG-NUP filaments twisting over each other to form a FG knot (solid yellow circle), Z-scale = 10 nm, speed = 5 frames/s) with 200 × 200 pixels. **(c)** Hiehgt profile of FG knots and single threads shown in this plot. **(d)** Heights of entangled FG-NUPs plotted against time to show dynamic and rapid conformations of Cobweb network; black arrows show highest and lowest FG-NUP heights observed at different conformational patterns. **(e)** Normal distribution curve of FG-NUP filament heights in d. **(f)** HS-AFM images showing two different conformations of the FG knot (central plug initiator). The upper image shows the cobweb pattern that represents the extended form of the FG knot. The lower image shows the random pattern of the FG network, indicating the conformation is reversible, (Z-scale = 10 nm, speed = 2.1 frames/s) with 200 × 200 pixels. (Figure S9, Supporting Information). (For interpretation of the references to color in this figure legend, the reader is referred to the Web version of this article.)

[7–9].

Direct visualization of the nanoscopic morphology of FG-NUPs is very difficult by conventional methods. This problem stems from the fact that IDPs including FG-NUPs are very thin and highly mobile, and thus electron microscopy (EM) or expansion microscopy and lattice light-sheet microscopy (ExLLSM) techniques are incapable of visualizing these protein [10–12]. IDPs containing IDRs are barely crystallized and hence X-ray crystallography is futile. Atomic force microscopy (AFM) can observe individual nanometer-scale objects under various environments [10,11]. However, the imaging rate of AFM is too slow to capture highly mobile IDRs in aqueous solutions [13]. This lack of imaging tools has limited the high-resolution visualization of the physical native structure of FG-NUPs in individual NPCs at the nanoscale resolution. High speed Atomic Force Microscopy (HS-AFM) has been previously used for the observation of dynamic behavior of several proteins in action [14,15]. Recently, we and others successfully used HS-AFM to visualize native NPCs in Xenopus eggs [16] and cancer cells [17]. In this work, we further explored the topology of native nanoscopic FG-NUPs of NPCs in colorectal normal cells, cancer cells and oncogenic colorectal organoids [18] using HS-AFM.

2. Materials and methods

2.1. Cantilever tip fabrication

Small custom-made cantilevers (BL-AC10DS, Olympus) with a spring constant k of approximately 0.1 N/m and a resonance frequency f = 1.5 MHz in water were used as mechanical probes. A long, sharpened carbon tip was grown on the top of each cantilever by electron beam deposition using a scanning electron microscope electron beam (ELS-7500, Elionix), as described previously [17]. Floor noise of HS-AFM has been excluded by measuring the height fluctuations over the elapsed time using the poly-L-lysine (PLL) substrate as a control. When comparing with FG-NUPs and CPs height fluctuations, it is clear that PLL has no significant changes (stable height). However, FG-NUPs and CPs showed wide range of height fluctuations. Therefore, we could exclude the hypothesis that height changes is due to HS-AFM noise (Figure S1).

2.2. FG-NUP analysis

The FG-NUPs network inside the NPC central channel was observed and analyzed in a speed of 100 ms/frame to scan a 40 × 40 nm^2 area inside the central channel. The image resolution varied according to stability, tip quality and sample roughness, and the FG-NUP data shown here were representative of our best resolved data. A fast Fourier transform (FFT) bandpass filter was applied with a maximum of 20 pixels for large structures, a minimum of 3 pixels for small structures and a tolerance of 5%. FFT processing was used only to filter large and small structures to see the tiny FG-NUPs. Later processing of the original data was used to observe the FG-Nups over different time points using image lookup tables. FG knot tracking was processed using ImageJ/MTrackJ software (imagej.nih.gov/ij/).

2.3. Measuring the extension velocity of FG-NUP filaments

The length-change of individual single FG-NUP filaments was measured in ImageJ by measuring the filament length over the elapsed time. The extension velocity was calculated according to the following equations:

$$\Delta L = L2 - L1 \text{ nm} \quad (1)$$

$$V = \Delta L / \Delta t \text{ nm/ms} \quad (2)$$

2.4. Measuring bending angles of FG-NUP filaments

The bending angles of FG-NUP filaments in different cell types was measured using the angle tool in ImageJ by measuring the bending from the NPC scaffold axis, as shown in Fig. 1G. The angle ϕ is the counter-clockwise measured angle between the x axis and the projection of the normal to the xy plane. Individual single FG-NUP filaments were tracked over the elapsed time to demonstrate the angular velocity ω between different time points according to the following equation:

$$\omega = \Delta\Phi / \Delta t \quad (3)$$

The clearest single filaments were selected for analysis of bending and motion. Other entangled filaments were excluded because of the difficulty to track bending from one time point to another.

2.5. FG knot formation tracking

The ImageJ/MTrackJ tracking tool was used to track the rapidly formed transient FG-NUP knots inside the native NPCs. The tracking trajectory positions indicated the different positions of FG knots (reversible). FG-NUP filaments overlapped to form FG knots. This tracking demonstrated the rapid reversible conformations between the knot and filamentous patterns of FG-NUPs.

2.6. Morphology and mobility analysis

Surface rendering of HS-AFM time series and manual 2D tracking of FG nups were performed in IMARIS 8.3 with Measurement Pro plugin (Bitplane, Oxford Instruments). Mean square displacement (MSD) curves were averaged from the displacement curves of identified individual FG nups. Diffusion coefficient was extrapolated from linear regression fitting of MSD curves, as $y = ax + b$, where a = diffusion coefficient [42]. Statistical analysis was performed using Prism 6 (Graphpad). Results are presented as mean ± sem. Normality tests (D'Agostino and Pearson omnibus or Shapiro-Wilk) were performed on all data sets. According to normality test results, data sets were analyzed either by unpaired *t*-test or by Kolmogorov-Smirnov test.

2.7. Cell culture, western blotting, immunoprecipitation and chromatin immunoprecipitation assay

These techniques were performed as described previously [43–45]. Briefly, Human colon cancer HCT116 cells were obtained from the American Type Culture Collection (ATCC) and were grown in Dulbecco's modified Eagle's medium (DMEM) supplemented with 10% (v/v) fetal bovine serum (Life Technologies) and 50 U/mL penicillin–streptomycin (Nacalai Tesque). For western blotting, cells were lysed with lysis buffer (20 mM HEPES (pH 7.4), 350 mM sodium chloride, 1.5 mM magnesium chloride, 1 mM EGTA, 10% (v/v) glycerol, 1% Triton X-100, a mixture of protease inhibitors (Roche), 0.2 mM sodium orthovanadate, and 1 mM phenylmethylsulfonyl fluoride). Samples were subjected to SDS-PAGE followed by conventional wet transfer. Membranes were incubated with primary antibodies and exposed to secondary horseradish peroxidase-conjugated antibodies (Millipore). Images were detected by using an LAS-4000 image analyzer (Fujifilm). For immunoprecipitation, samples were further washed three times with lysis buffer and Dynabeads Protein A/G (VERITUS, Tokyo, Japan) were added. After 2 h, beads were washed four times in IP buffer (50 mM Tris, pH 7.6, 100 mM NaCl, 2 mM EDTA, 0.2% Nonidet P-40) and then subjected to Western blot. For His-tag pull-down assay, all steps were performed following the manufacturer's protocol (DynabeadsTM, His-Tag Isolation & Pulldown, 10103D, Invitrogen). For chromatin immunoprecipitation assay (ChIP), Formaldehyde was used to cross-link proteins to DNA. Cells were lysed with buffer A (10 mM HEPES, pH 7.9, 10 mM KCl, 0.1 mM EDTA. 0.1 mM EGTA, 0.5% NP-40). Nuclei were pelleted at 12 000 rpm for 5 min and lysed in 800 µl lysis buffer (50 mM Tris-HCl, pH 8.0, 10 mM EDTA, 1% SDS). Cell lysates were sonicated using a Bioruptor ultrasonic cell disruptor to shear genomic DNA to an average fragment size of 150–250 bp, and immunoprecipitation was performed using Chip-grad antibody.

2.8. Reagents

DIF-1 (differentiation-inducing factor-1) was purchased from Sigma (SML0599). CHD (*trans*-1,2-cyclohexanediol) was obtained from Tokyo Chemical Industry CO., LTD (C0809). Antibodies anti-beta-catenin (#8480) and anti-TCF7L2/TCF4 (#2569) were purchased from Cell Signaling and anti-β-actin (sc-47778) was obtained from Santa Cruz. Anti-FG-NUPs (M414) was purchased from COVANCE (MMS-120R).

2.9. Cell proliferation assay

Cells were seeded into a 96-well plate at 3000 cells/well and cultured for the indicated times. Cell viability was assessed using the MTT (3–4, 5-dimethylthiazol-2-yl) −2, 5-diphenyltetrazolium bromide) method. In brief, 10 µL of 12 mM MTT solution was added into each well, followed by 3 h incubation. The reaction stopped by adding 100 µL of STOP solution (2% acetic acid, 16% SDS, 42% DMF). Samples were mixed thoroughly and measured at 570 nm for absorbance.

2.10. Soft agar colony formation assay

The basal layer was prepared by mixing an equal volume of 1.25% (wt/vol) agarose (DNA grade) with 2X DMEM plus 20% (vol/vol) FBS. The top layer was prepared by mixing an equal volume of 0.75% (wt/vol) low-melting agarose with 2X DMEM plus 20% (vol/vol) FBS. The basal layer mixture was added into each well of a 12-well plate and allowed to solidify before cell seeding. An appropriate amount of cells was added into 0.5 ml of the pre-warmed top layer mixture and overlaid onto the basal layer. Feeder medium was added after the top layer solidified. After 3–5 weeks, colonies were stained using 0.2% (wt/vol) crystal violet in 4% (wt/vol) paraformaldehyde and then photographed using a dissecting microscope.

2.11. Migration assay

CRC cells were seeded onto transwell inserts (3422, Corning, Kennebunk, ME, USA) in 24-well plates and incubated for 20 h. The inserts were washed with PBS, and non-migrating cells were wiped off the top side of the insert. Migrated cells were fixed and stained with 0.2% (wt/vol) crystal violet in 4% (wt/vol) paraformaldehyde. The numbers of migrated cells were counted by microscope observation.

2.12. cDNA preparation and quantitative real-time RT-PCR assay

We used 500 ng RNA for cDNA preparation using ReverTra Ace® qPCR RT Master Mix (TOYOBO). Quantitative real time RT-PCR was performed using SYBR® Premix Ex Taq™ II (Takara) in a Thermal Cycler Dice® Real Time System (Takara) according to the manufacturer's instructions. The relative mRNA expression levels of target genes were calculated using ACTNB as a loading control.

2.13. Transfections, viral particle production and infection

DNA and siRNA transfections were performed using Lipofectamine 2000 and Lipofectamine RNAiMAX (Life Technologies, Carlsbad, CA, USA), respectively. Lentiviral particles were produced with the

MISSION Lentiviral Packaging System (Sigma-Aldrich). CRC cells were transduced with the lentiviral particles in the presence of 8 μg/ml polybrene (Sigma-Aldrich) for 48 h.

2.14. shRNA vectors

The shRNA construct for NUP214 (target sequence: CCATAGAATC TCACACCAAAT) was constructed with PLKO.1 as backbone using *Age*I and *Eco*R I sites.

2.15. URLs

Integrated Genomics Viewer (IGV), http://www.broadinstitute.org/igv; cBio Cancer Genomics Portal, http://www.cbioportal.org/; Gene Expression Omnibus (GEO), http://www.ncbi.nlm.nih.gov/geo/; Cistrome DB, http://cistrome.org/db/.

2.16. Super resolution microscopy (STED)

Samples were prepared on chamber slides and fixed for antibody reaction processes. For organoid structure determination, confocal z stacks were acquired at an optical resolution of 1024 × 1024 with an optical z slice every 1 μm for 40 × images (Leica SP8). High-resolution imaging was performed on a STED microscope (Leica SP8 STED; 100 × oil immersion objective, N.A. 1.4) and operated with the Leica LASX software. Deconvolution of raw images was performed using Huygens professional software.

2.17. Optical diffraction tomography (ODT) analysis

Three-dimensional refractive index maps were obtained for CRC cells during CHD treatment using ODT. The acquisition and analysis of images were performed according to the manufacturer's instructions (TomoStudio™, Tomocube Inc., Republic of Korea).

2.18. Statistical analysis

Statistical analyses were done in Excel. Data are shown as mean ± SD. Comparisons between groups were resolved using the unpaired *t*-test. $P < 0.05$ was considered statistically significant. IBM SPSS Statistics 25 was used for normal distribution curve preparation.

2.19. Data availability

The data that support the plots within this paper and other findings of this study are available from the corresponding author upon reasonable request.

3. Results and discussion

3.1. FG-NUPs conformations in colorectal cancer cells

FG-NUPs of the selective barrier of NPC were visualized in this study to demonstrate their interactions and working model. These nanoscopic studies raise the possibility of using HS-AFM to solve two key questions in the NPC field. 1) How do FG-NUPs interact with one another, affording them a certain LLPS 'cohesiveness' [21]: whether more cohesive FG-NUPs form more compact "mesh-like" morphologies and less cohesive FG-NUPs form more extended morphologies? 2) NPC central filaments undergo a frequent extend and retract writhing in the central NPC cobweb and recalled another most controversial structural feature of the NPC: the CP [1,4,7,10], a large mass observed in the center of many but not all NPCs [22]. This prompted us to consider a long-standing question in the NPC field: how is the CP formed? There are several different hypothesis and models on the function and composition of those central granules as FG-NUPs components of the NPC or "CPs" [8,9] or "transporter" (CP/T) or "cargoes in transit" [1] or some peptides related to diseases that block the central channel of NPC [23]. However, specific *in vitro* evidence has been lacking. To address this question, we used HS-AFM to visualize filaments extend and retract writhing in the central cobweb of NPCs in HCT116 colorectal cancer cells. First we traced the rapid conformations of symmetric outer ring scaffold and we demonstrated a fuse/separate dynamic pattern between individual cytoplasmic filaments (Fig. 1a, Figure S2 and Video S3B, Supporting Information). This pattern in turn leads to rapid changes in the inner lumen and its FG NUP network. Interestingly, we can demonstrate that the outer scaffold side with rapid conformations emerged many extended FG-NUP filaments with a brushes pattern. However, the outer scaffold sides with less conformations, its FG-NUP filaments are more retracted aside (Figure S3 and Video S3C, Supporting Information). Fig. 1b shows FG-NUP filaments twisting over each other and rapid formation of transient loops and hitch. The FG-NUP filaments interacted in a very dynamic and reversible behavior. This interaction could form the complicated entanglement of the cobweb or single filaments can overlap and twist over each other to form thick transient knots (Figure S4-5 and Video S3a¬f, Supporting Information). To more closely examine the transient FG knots, we plotted the x-y directional displacement and height and found that two single filaments (single filament thickness, ~0.9 nm) twisted to form the thick knot (thickness, 1.5–4.3 nm) (Fig. 1b-e, Figure S5 and Video S3d, e, Supporting Information). We found that these knots were considerably smaller in size than the hydrodiameters of a karyopherin (~10 nm) or large cargo (> 5 nm) and should not injudicious for cargoes in transit [16,24]. Therefore, these transient FG knots might be the initiators or precursors for CP formation. In addition, the FG-NUP network conformations involved the reversible formation of several pores in a transient "mesh-like pattern" that is not clear in most FG-NUP recordings because of the cloudy entanglements of FG-NUP filaments (Figure S6–8 and Video S4a–c, Supporting Information). The average mesh diameter was 6.3 ± 4.2 nm (n = 30). Other HS-AFM recordings showed the FG knot with its IDP nature can be condensed (thickness, ~2.9 nm) to a narrow area at the center of the NPC lumen or can be reversed to be a flattened knot (thickness, ~1.7 nm) with many FG-NUP filaments connected around it. These FG filaments resilience dynamic process was rescindable (Fig. 1f, Figure S9 and Video S4a, Supporting Information). Thus, these observations confirm the flexible IDP nature of FG-NUPs and show that their shape and thickness can be modulated to a variety of patterns.

Supplementary video related to this article can be found at doi:10.1016/j.biomaterials.2020.120198

3.2. Nanoscopic inner nuclear pore morphology in normal colon cells

To examine the nanoscopic inner nuclear pore morphology in normal colon cells, we first visualized the nuclear pore dynamics in normal colon CCD18CO cells. We found an individual NPC averaged over 150 frames recorded at 3.3 frames per second by HS-AFM (Figure S3, Supporting Information). The NPC showed an average diameter of 74 ± 18 nm and average depth of 4.8 ± 2.5 nm (n = 81) (Fig. 2a, Figure S10, and Video S1A, B, Supporting Information). We did not find significant differences in NPC diameter and depth between normal and cancer cells (Figure S3, Supporting Information). Since the morphology of FG-NUPs in the central lumen is of great importance for understanding the mechanism of selective transport through the NPC, we next conducted analysis of FG-NUP single filaments in normal CCD18CO colon cells. Similar to the diffusive motion of IDPs and our results in HCT116 cells [17], we recorded successive HS-AFM images that exhibited distinct structures of FG-NUPs in the central after we raised the scan rate to 3.3 frame/s (300 ms/frame). Interestingly, FG-NUPs were concentrated forming bristle in a writhe-like cobweb manner from their tethering points that were located closer to the nuclear periphery (Fig. 2b and Video S1C, D, Supporting Information). We

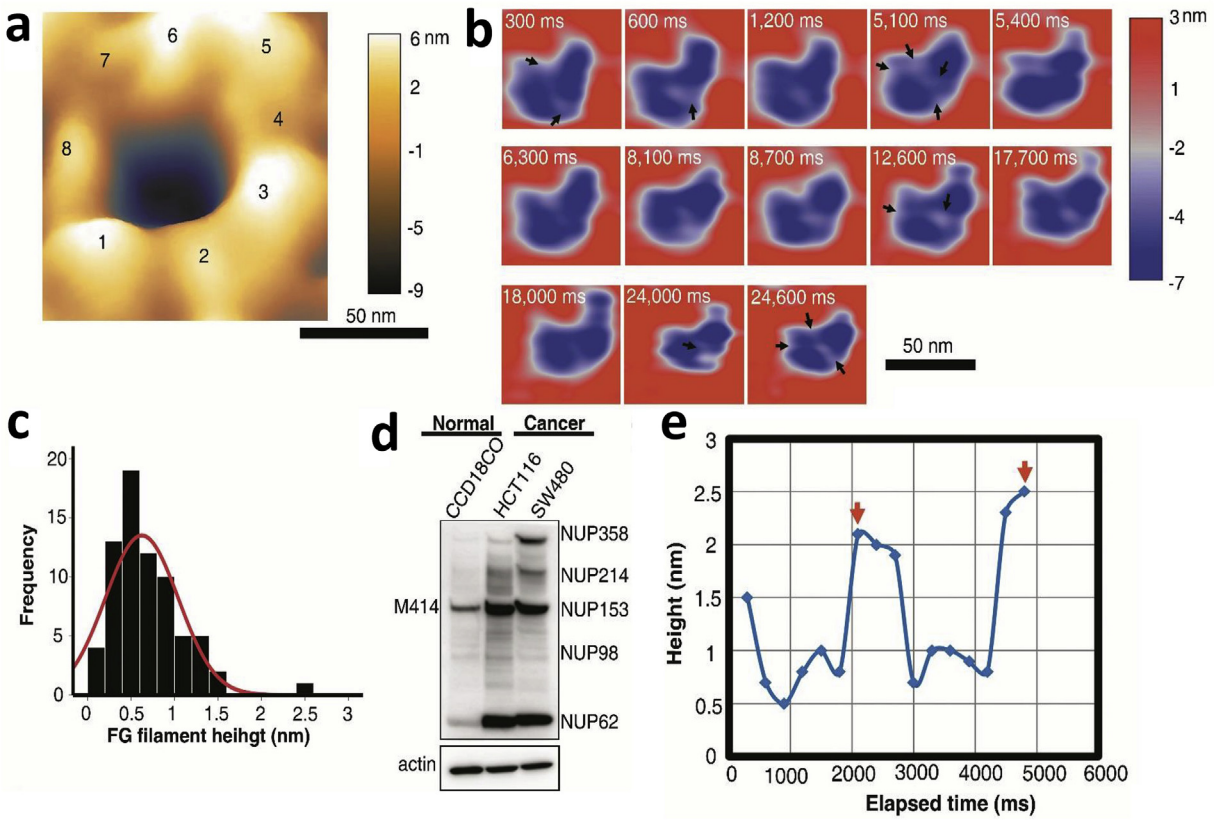

Fig. 2. FG-NUP single filament tracking in NPCs from healthy and cancerous colon cells. (a) HS-AFM image of a representative single NPC of CCD18CO cells rendered in 3D format showing symmetric cytoplasmic filaments. **(b)** Successive HS-AFM images showing FG-NUP filament dynamics inside the native central channel of CCD18CO cells. Black arrows indicate single filaments extending from their tethering points at the NPC scaffold. Z-range is 13 nm, scanning speed is 3.3 frames per second, 200 × 200 pixels. **(c)** Normal distribution curve of FG-NUP filament heights. **(d)** Western blot analysis of m414 in the indicated cells. **(e)** Single FG filament height plotted against time in CCD18CO NPCs. Red arrows indicate two thick FG-NUP aggregates near the inner channel wall. (For interpretation of the references to color in this figure legend, the reader is referred to the Web version of this article.)

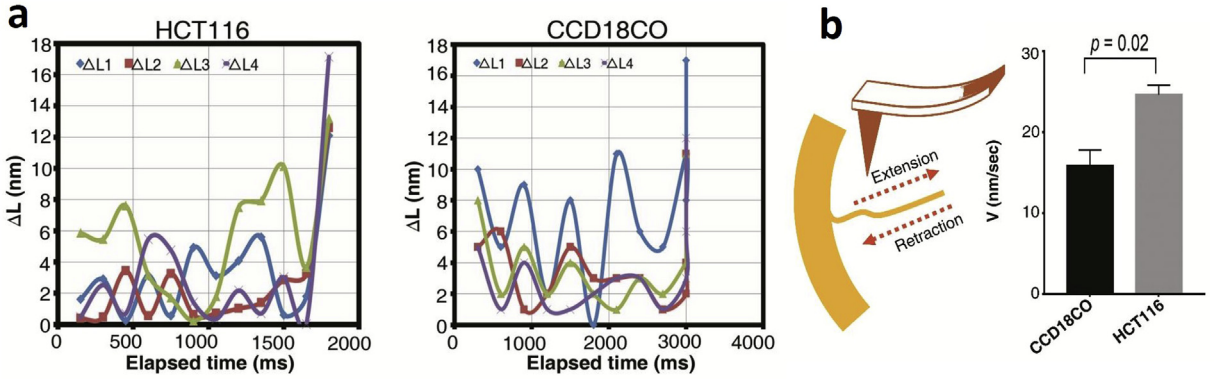

Fig. 3. Extension velocity of single FG-NUP filaments. (a) Individual FG filament length-change velocity is measured by calculating the length-change over different time points in both CCD18CO and HCT116 cells (N = 4). The length in nm is displayed from the tethering point to the free end for each single filament. Only the very clear single filaments have been selected for this measurement and the entangled intra-network filaments have been excluded. **(b)** Individual FG filament length-change velocity measured by calculating the length-change over time in CCD18CO and HCT116 cells.

rarely found the swaying motion of extended FG-NUPs that coincide and intermingle in the central whip gelatin like protrusion filaments in normal CCD18CO colon cells compared with those in HCT116 cells (n = 50). The average single FG filament height was ~0.6 ± 0.4 nm (n = 71) in normal CCD18CO colon cells (Fig. 2c). Consistent with these results, FG-NUPs were up-regulated in colon cancer cells compared with normal CCD18CO cells (Fig. 2d) and FG-NUP aggregates were observed near the inner channel wall in NPCs in normal CCD18CO cells (red arrows in Fig. 2e). Morphological and dynamic analysis show that NPC in colorectal cancer samples have a significant reduction in their surface area (Figure S11a-b, Supporting Information) and display an increase in the number of FG nups protrusions in the central core of the pore compared to control CCD18CO samples (Figure S11, Supporting Information), leading to a significant alteration of the sphericity/ellipticity of the NPC in colorectal cancer (Figure S11c-d, Supporting Information).

3.3. Tracking of FG-NUP single filaments

Understanding of the mechanics and dynamics of biofilaments has

been studied intensively for the last decades with different conceptual considerations [32]. A long flexible filament like FG-NUPs can have a number of possible internal structures. In the position where the FG-NUPs are highly condensed, the complex topological patterns like knots or entanglements are naturally emerging. The existence of knotting in a filament naturally affects its configuration and physical properties [33,34] as shown in Fig. 1.

To further distinguish the nanoscopic behavior of single filaments between normal and cancer colon cells, we next calculated the change in filament length over time and measured the rate of stretching of a single FG filament. We found that the extension velocity of single FG filaments in normal cells was much slower than in cancer cells (Fig. 3a–b; $P = 0.02$). We also calculated the length vagaries over time and the rate of velocity changes of single FG filaments during extension. As expected, the extension velocity of single FG filaments in cancer cells was significantly higher than in normal colon CCD18CO cells ($P = 0.02$). Next, we compared the bending angles of single filaments inside the central channel of normal and cancer cells. FG-NUP filaments bend in two different directions away from their tethering points. These bending angles were calculated to determine the degree of bending from the NPC scaffold axis using ImageJ software (Fig. 4a–c and Figure S12, Supporting Information). We calculated the FG-NUP filament bending angle plotted against time to track the bending of single filaments away from the scaffold NPC. We also estimated the different bending angles of filaments in HCT116 and CCD18CO cells; the average bending angle was ~153 ± 43° in HCT116 cells (n = 45) and ~140 ± 25° in CCD18CO cells (n = 45) (Fig. 4, Figure S12 and Video S2, Supporting Information). In HCT116 cells, the highest frequency of bending filaments was detected in the 170–180° fraction, which corresponded to the extended filaments. A small fraction of filaments with very narrow bending angles was also observed, which correspond to the bending of filaments in the opposite direction, indicating the high flexibility of filaments in HCT116 cells. Our HS-AFM movies thus revealed that FG-NUPs occluding the central transport channel of the NPC are natively disordered and demonstrate the different FG-NUPs filament moving behaviors between normal and cancer cells in terms of conformational variability or rotational rearrangements speed and bending angles within the observation time windows. These data support the idea that FG-NUPs close to the nuclear periphery may function as a part of the transport barrier [19] and also act as a nucleation site for proteins required for the active transport of macromolecules in normal colon cells [20].

3.4. Dissection of FG-NUP single filaments

Our initiatory study to capture and manipulate single FG-NUP filaments in their native environment in normal and cancer cells since tracking the dynamics of such nano-biofilaments is challenging. To explain the different patterns of bending of single filaments in normal and cancer; we further applied the dissection model by taking five cross sections at the entire length of single filaments in both normal and cancer models as shown in Fig. 5a. The results showing that single

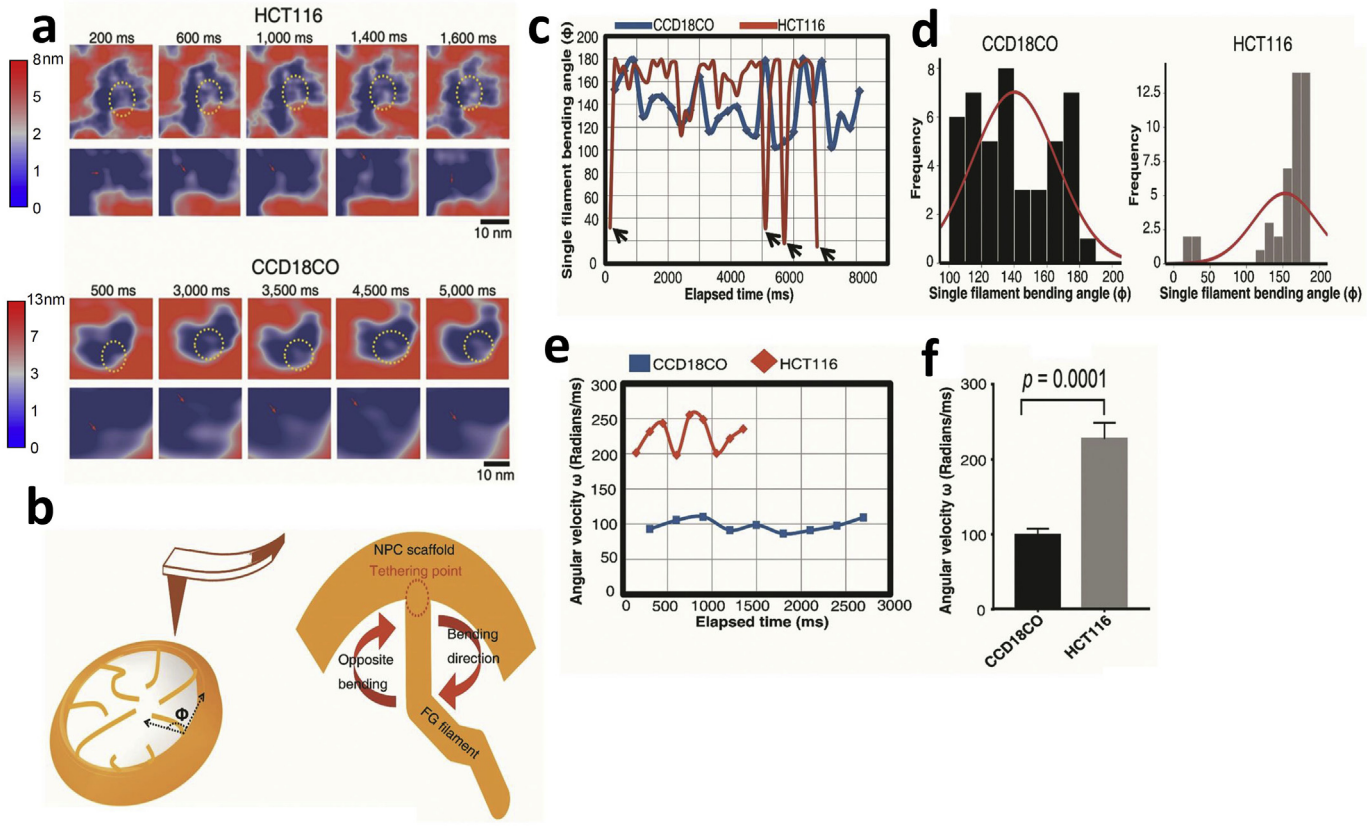

Fig. 4. Single FG filament bending in native NPCs of HCT116 and CCD18CO cells. (a) HS-AFM images of the native central channel are shown with the tracking of single FG NUP filaments in HCT116 (upper panel) and CCD18CO (lower panel) cells. Successive frames of a native NPC central channel showing the wide ranged bending ability of FG filaments in different directions in cancer cells but limited bending ability in normal colon cell. Scale bar, 10 nm. Imaging parameters for HCT116; Z-scale = 8 nm, speed = 1.2 frames/s, with 200 × 200 pixels. Imaging parameters for CCD18CO; Z-scale = 13 nm, speed = 3.3 frames/s, with 200 × 200 pixels. **(b)** Bending possibilities of FG-NUP filaments in two different directions away from their tethering points. Diagram on the right shows extending and retracting FG filaments inside the central channel of NPC and bending angle measurements. **(c)** FG-NUP filament bending angle (Φ) plotted against the elapsed time to track the bending of single filaments away from the scaffold NPC. Plot shows the different bending angles of HCT116 (n = 45) and CCD18CO cells (n = 45). Black arrows indicate bending happening in the opposite direction of all other bending points. **(d)** Normal distribution curve of FG-NUP filament bending angles in CCD18CO and HCT116 cells. **(e, f)** Angular velocity of individual FG filaments in CCD18CO and HCT116 cells as calculated from the same filaments shown in **c**.

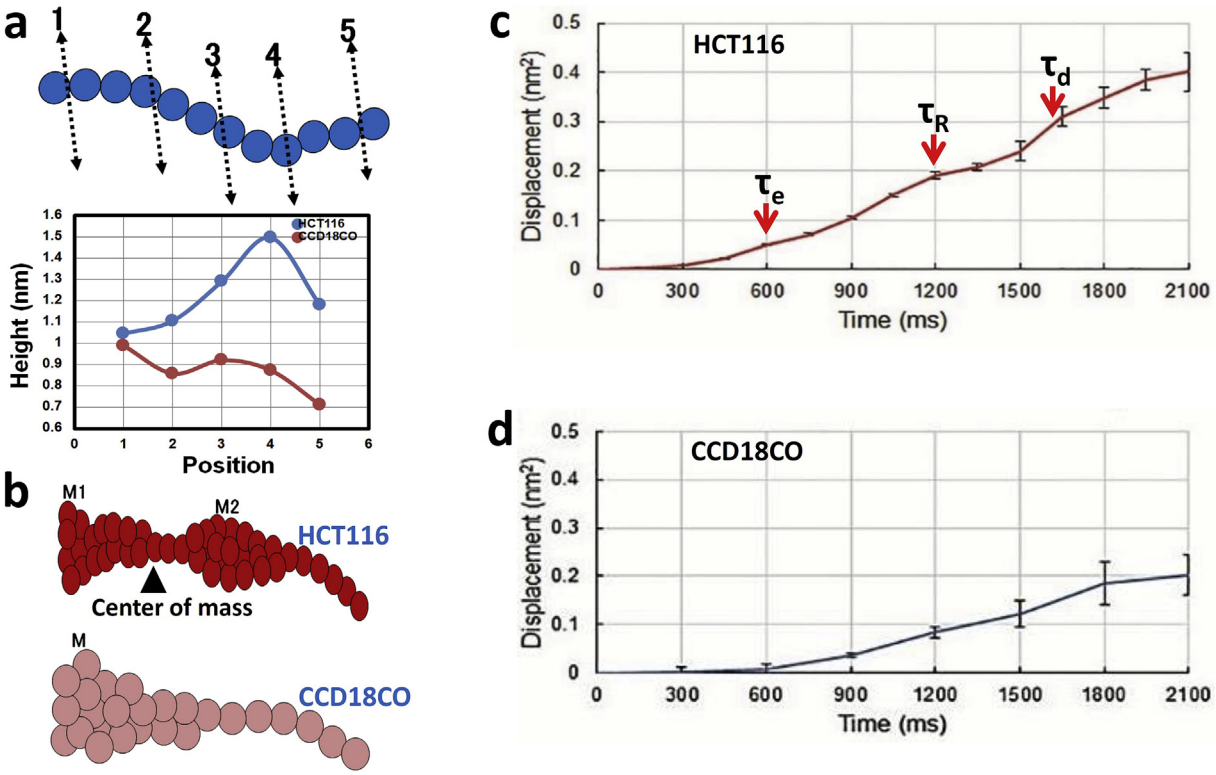

Fig. 5. FG-NUP dissection and reptation dynamics. (a) FG-NUP single filament dissection analysis achieved by taking five cross sections at different points of the entire length of single filament. The cross section plot below is showing the thickness of each point of single filaments in both CCD18CO and HCT116 cells (N = 10). **(b)** FG-NUP filaments in HCT116 cells showing heterogeneous thickness along the entire length which resulted in two main knots (M1, M2) at different points, which formed the center of mass (CM) between M1 and M2. Therefore, a balanced motion and bending achieved. On the other hand, CCD18CO cells showing homogenous thickness along the entire length of FG-NUP filament except for one knot at the tethering point (M), which keep the filament with less motion and less flexibility to bend. **(c)** The reptational motion of flexible chains is characterized by the mean square displacement (MSD) which shows four different kinetic regimes. At short times the filament motion is controlled by free Rouse dynamics. After the entanglement time (τe), the filament is confined by the nearby filaments. At Rouse time (τR), the internal degrees of freedom are relaxed but the filament still confined. After the reptation time (τd), Fickian diffusion is observed. Altogether these data reveal a substantial increase in the dynamic behavior of FG filaments inside the inner lumen of NPC in HCT116 colon cancer cells. **(d)** These different kinetic regimes were not clearly determined from the MSD analysis in CCD18CO filaments. See full tracking results in Figure S12.

filaments in cancer cells have a heterougenous thickness along the entire length. The filament has several thick points (knots); one at the tetring point and one at position 4. So, the center of mass is residing between these two knots, which increase the flexibility of the filament and can give a balance during the bending (Fig. 5a–b). On the other hand, in normal cells, the single filaments appeared as a broken stake with a decreasing thickness in the direction of the free end, which facilitate only the passive swimming of the filaments and hardly to bend in different directions. (Fig. 5a–b and Video S2, Supporting Information). To date, it is difficult to track and manipulate such disorederd FG-filaments in their entangeled state. Furthermore, it is hard to apply the previous biofilament or polymer mathematical models to these filaments [35]. Taken together, the current dissection model of single FG-NUP filaments is a tentative model to explain the HS-AFM microscopic tracking and manipulation of such disordered-entangeled filaments. In addition, this model awaits for future mathematical and biophysical validation.

3.5. Reptation dynamics of confined FG-NUPs

FG-NUP filaments observed in the native NPCs are considered as flexible polymers. The motion of a linear polymer chain under entangled conditions has been explained by the reptation theory [36]. Reptation model has been confirmed for linear chains using natural polymers such as DNA [37] and actin filament [38] as well as synthetic polymers [39]. In these studies, although motion and conformational state of single chain were captured directly, quantitative analyses were often conducted based on overall motion and relaxation of the chains such as chain-length-dependent motion of center of mass (CM) (Fig. 5a–b). Here, we provided a single filament tracking of FG-NUPs to determine the motion pattern of these filaments in terms of space and time. The elongation as well as the bending angles of FG-NUPs in colorectal cancer also rise significantly (Figure S12a-e, Supporting Information) indicating that the movements of FG-NUPs protrusions become more dynamic and complex in NPC from colorectal cancer compared to control samples. The rise in FG-NUPs mobility in colorectal cancer was additionally confirmed by 2 times increase in FG-NUPs diffusion coefficient in cancer compared to control samples (Fig. 5c–d and Figure S12f-h, Supporting Information). The reptational motion of flexible chains is usually characterized by the mean square displacement (MSD) which shows four different kinetic regimes. At short time intervals the filament motion is controlled by free Rouse dynamics. After the entanglement time (τ_e), the filament is confined by the nearby filaments. At Rouse time (τ_R), the internal degrees of freedom are relaxed but the filament still confined. After the reptation time (τ_d), Fickian diffusion is observed [36]. Altogether these data reveal a substantial increase in the dynamic behavior of FG filaments inside the inner lumen of NPC in HCT116 colon cancer cells.

3.6. Dynamics of native central plug

From the EM micrograph, we found that ~25% of NPCs in colorectal cancer (CRC) were plugged in HCT116 cells (n = 492) and ~10% in normal colon cells (n = 590) (Figure S13, Supporting Information).

Therefore, we used HS-AFM imaging to further visualize any changes to NPCs with CPs in normal and colon cancer cells (Figure S14, and Figure S15, Supporting Information). To further determine the physical and dynamic properties of the CP, we compared native structural dynamics of CPs in normal and cancer colon cells. The most obvious difference was that the CP in CRC HCT116 cells was almost ~3-fold higher than that in normal colon cells (Figure S14, Supporting Information). In addition, the CP phonologically shape confrontational changes in cancer were more than in normal cells. In addition, the CP in cancer cells showed more FG connectors extending to the outer ring (Figure S14, Figure S15 and Video S5, Supporting Information). Together with cross-sectional analysis and elapsed time measurement of CP, we demonstrate that the CP has no static and definite shape [1,4,7,10] (Figure S15f, Supporting Information). Unlike other microscopy methods that rely on ensemble averaging for obtaining nanometer-range resolution [9,25], our HS-AFM movies showed that FG filaments undergo substantial confrontational changes in structure and dynamics in length and height, squirming and twisting during their interaction; in combination with their thickness undergoing rapid conformation, these filaments spatiotemporally form reversible small clumped hitches and knots that resemble CP precursors that might ultimately give rise to a quintessential CP in the NPC lumen of both normal and cancerous colon cells.

3.7. Clinical embroilment of FG-NUPs in colorectal cancer

The above data prompted us to further investigate the direct contribution of FG-NUPs in colorectal cancer (CRC). We compared the expression profiles of FG-NUPs in normal versus CRC tumor samples using cDNA microarray data from Gene Expression Omunibus (GEO; series GSE8671). We found that FG-NUPs are over-expressed in CRC (Fig. 6a). Previous studies demonstrated that the transcription factors CTNNB1 and TCF7L2 are master oncoproteins that affect CRC initiation and progression [26,27]. However, the involvement of these transcription factors in regulating the expressions of FG-NUPs remains unknown. We first re-analyzed chromatin immunoprecipitation-seq data (GSE31477) and found that TCF7L2 binds the promoter region of the NUP214 gene in HCT116 cells (Figure S16, Supporting Information). Consistent with previous studies [26,27], TCF7L2 formed a complex with CTNNB1 (Figure S17, Supporting Information). Of note, the mRNA levels of NUP214 were decreased upon either CTNNB1 silencing (GSE87429) or expression of mutant TCF7L2 (GSE18560), suggesting that CTNNB1 and TCF7L2 regulate NUP214 expression together (Figure S17, Supporting Information). Notably, Kaplan-Meier analysis on the TCGA cohort revealed that the upregulation of NUP214 was significantly correlated with poor outcome of CRC patients (Fig. 6b).

Since DIF-I (a cell proliferation inhibitor) inhibits both CTNNB1 and TCF7L2 expression levels *in vitro* and *vivo* [26,27], we next analyzed the expression levels of FG-NUPs in organoids after DIF-I treatment. Consistent with previous findings, DIF-I decreased the levels of CTNNB1 and TCF7L2 in both cell lines (Figure S18, Supporting Information) and organoids (Fig. 6c). Organoids [28] treated with DIF-I show a smooth appearance, whereas untreated organoids have a folded surface (Fig. 6d and Video S6, Supporting Information). Importantly, both mRNA and protein levels of several FG-NUPs, including NUP214, were significantly decreased after DIF-I treatment (Fig. 6e–f and Figure S18, Supporting Information). Furthermore, stimulated emission depletion (STED) imaging revealed that DIF-I-treated organoids showed decreased levels of FG-NUPs and defects in nuclear envelope formation (Fig. 6g). Finally, we investigated whether NUP214, the candidate FG-NUP downstream of CTNNB1/TCF7L2, is involved in CRC biology. We established HCT116 cells expressing shNUP214 (Fig. 6h). Consecutive HS-AFM images revealed that silencing NUP214 was sufficient to compromise and alter the symmetric distribution of outer cytoplasmic filaments in HCT116 cells (Fig. 6i–k, Figure S19 and Video S7a, b, Supporting Information). In addition, the abnormal distribution of FG filaments was retracted to the outer ring without movements observed in control colon cells. This abnormal dynamic behavior of FG-NUPs might be due to the defects in the outer scaffold of NPC (Fig. 6j, Figure S19 and Video S7C, Supporting Information). We also found that HCT116 cells silenced for NUP214 lost malignant phenotypes, including proliferation and migration (Fig. 6k–m). These data strongly indicate the clinical significance of the IDP FG-NUP214 in CRC initiation and progression. Together, using IDP FG-NUP214 as a nucleoporin example, we used *in vitro*, *in vivo* and *in silico* data to demonstrate that the expression and nanoscopic dynamics of FG-NUPs are critical in CRC carcinogenesis.

Based on the above functional data, we further using HS-AFM to visualize the ultrastructure of individual FG-NUPs after treating HCT116 cells with 3% 1,2-hexanediol (CHD) for 48 h. CHD is used to disrupt the FG-NUP permeability barrier because it can interrupt the hydrophobic interactions between FG repeats [29,30,39,50–52]. We first applied holo-tomography techniques and found that, as predicted, CHD treatment induced nuclear degradation in different CRC cells (Figure S20 and Video S8, Supporting Information). HS-AFM successive images revealed the effect of CHD on FG-NUPs filaments inside the central channel, showing retraction to the edge. Moreover, CHD-treated cells showed prominent dilated and reamed central lumen structures of NPC in a time-dependent manner (Fig. 7a and b, Figure S20 and Video S9–10, Supporting Information). This phenomenon was further confirmed by measurement of individual FG height (n = 43) and angles (n = 14) (Fig. 7b). We also found that the FG-NUP bending angle range was fairly narrow (60°–140°). Strikingly, we also found a significantly reduction of CP using EM (Figure S13, Supporting Information) and found that several CPs were worn-out into smaller pieces by HS-AFM in HCT116 cells after CHD treatment (Fig. 7c and d and Video S10b, Supporting Information). These data hinted that CP components might be related to FG-NUP components. We next investigated the features of FG filaments and CPs in AKTP (a mouse metastatic intestinal cancer organoid which carry ApcΔ716 Kirsten rat sarcoma viral oncogene (Kras)G12D Tgfbr2−/− Trp53R270H mutations) organoids by recording successive HS-AFM images (Figure S21 and Video S9, Supporting Information). Amazingly, we clearly found that several CPs disassembled back into single FG filaments (Fig. 7e and f and Video S10c, Supporting Information). We then measured FG-NUPs connected to the CP and the difference in height of FG-NUPs before and after the destruction of the CP (Fig. 7g and h). Consistent with the organoid observations, FG filaments re-appeared and clearly connected with reaming FG knots (recalling the FG knots observed in HCT116 cells and recalling the cobweb network resembling [17]). The height of CPs was also reduced in AKTP organoids after CHD treatment (Fig. 7i and j). Since karyopherin-β and importin-β mainly facilitate import of cargoes in-transit to the NPC [31], to independently confirm the above observations, we also examined the effect of importazole (20 μM), which selectively blocks karyopherin-β-mediated nuclear import, on the CP using EM and HS-AFM. We found no significant effect of importazole on CP existence (Figure S13, Supporting Information) or height (Figure S22 and Video S10d, Supporting Information). We also checked the effect of high Ca^{2+} on the FG-NUPs conformations which resulted in phase separated FG-NUP particles, which finally aggregated forming thicker plug (Fig. 7k, Figure S23 and Video S11, Supporting information). Together, our study has clarified long standing questions in the NPC field and our findings demonstrate that the CP within the nuclear pore is at least partially constructed by FG-IDPs in cancer cells and organoids (Fig. 8).

4. Conclusion

X-ray crystallography, cryo-EM and, more recently, in-cell nuclear magnetic resonance have proven to be useful tools to study the structure-function relationships of NPCs at molecular levels [46,47]. These techniques depend on “average-out” imaging techniques and analyze

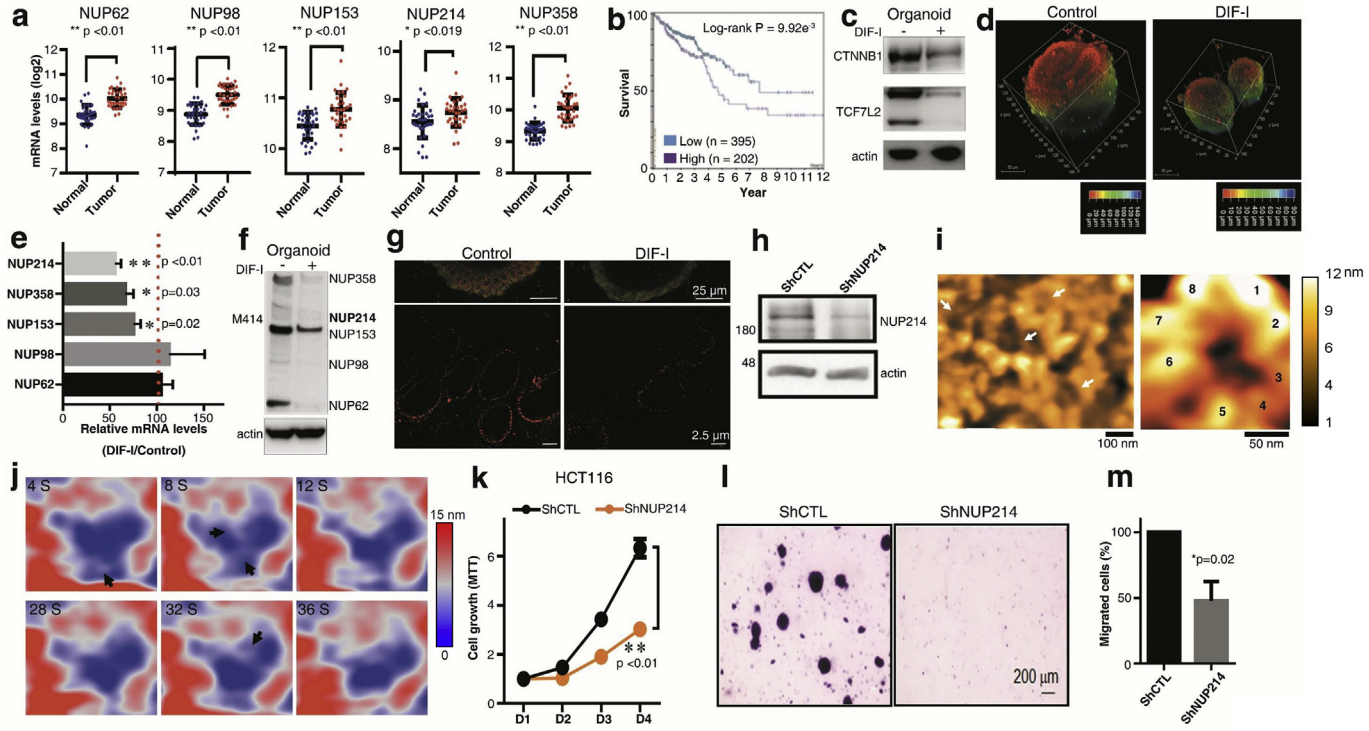

Fig. 6. Clinical importance of FG-NUPs in colorectal cancer. **(a)** FG-NUP mRNAs by RNA-seq in normal tissues compared with colorectal tumors from GEO (GSE8671). **(b)** High NUP214 expression was associated with poor survival of CRC patients in the TCGA cohorts. **(c)** Western blot analysis of CTNNB1 and TCF7L2 in organoids treated with DIF-I (30 µM, 48 h). **(d)** 3D imaging of organoids treated as indicated. **(e, f)** qRT-PCR **(e)** and Western blot analysis **(f)** of FG-NUPs in organoids after DIF-I treatment (30 µM, 48 h). **(g)** STED imaging of FG-NUPs in organoids treated as indicated. **(h)** Western blot analysis of NUP214 in HCT116 cells expressing NUP214 shRNA. **(i)** HS-AFM image of the cytoplasmic face of the nuclear envelope in HCT116 cells expressing NUP214 shRNA. Z-range is 13 nm, scanning speed is 0.4 frames per second, 200 × 200 pixels. White arrows indicate abnormal NPCs. The NPC on the right shows the abnormal structure of cytoplasmic filaments. **(j)** Successive HS-AFM images of the native central channel of HCT116 cells expressing NUP214 shRNA, showing the abnormal distribution of FG filaments that appeared more retracted to the outer scaffold. The abnormal behavior and motion of FG-NUPs are due to defects in the outer scaffold of NPC. Z-scale = 15 nm, speed = 0.4 frames/s, with 200 × 200 pixels. **(k, l)** MTT assay **(k)** and soft agarose colony formation assay **(m)** of NUP214-silenced HCT116 cells. Data are shown as mean ± SD from three independent experiments (n = 3). **(l)** Transwell migration assay in NUP214-silenced HCT116 cells. Data are shown as mean ± SD (n = 3).

the protein complex in a non-physiological environment given the motionless snapshots of immovable conformations, from which *in vivo* functional states can be difficult to investigate. HS-AFM has recently been applied for the visualization of biomolecules in dynamic action at a high spatiotemporal resolution without an impact on protein function [17]. Nevertheless, due to cantilever tip sizes and morphologies, immobilization strategies, native sample buffering, measurement conditions and other nanoscale mechanical parameters, the visualization of live intracellular organelles, such as the nucleus or mitochondria, has remained challenging [15]. In our previous report [17], we visualized native NPCs in HCT116 CRC cells using HS-AFM. We further proposed a "spiders cobweb" model for the process of central channel shuttling or gene gating by the nuclear pore. Recent study used AFM to observe the dynamics of IDPs from two systems: the transport barrier of native NPCs and the transport barrier of a mimetic NPC made using a DNA origami [48]. This study splendidly distinguished the dynamics of IDPs from other common AFM noise which can interfere with the rapid motion of IDPs. Inspiring their robust strategy, we avoided this possibility by measuring the HS-AFM noise floor (Figure S1 and Video S12, Supporting Information). In addition, we used a filtering protocol and template-match algorithm to remove thermal drift in x, y and z-directions [17]. Furthermore, the current HS-AFM has an advanced PID controller (named a dynamic PID controller) with a capability to automatically change the PID's gain parameters, depending on the cantilever oscillation amplitude to avoid the tip-parachuting effect and ensure stable imaging under a small tapping force which facilitated the tracking of tiny nano bio-filamnets of the NPCs in their native environment [17]. NPC outer ring is dynamic not static due to the self-arrangements of cytoplasmic filaments [49]. Also as shown in Figure S2 and Figure S3, NPC scaffold structural arrangements affected the central FG-NUP barrier dynamics and this confirm the hypothesis that the transport through NPC is governed by the overall dynamics of the NPC machinery. In addition, our findings on FG-IDP expression and dynamics have clinical importance. We also demonstrated that FG-NUP214 plays critical roles in the early stage of CRC carcinogenesis (Fig. 6).

Here we performed HS-AFM real-time imaging and found that FG-NUPs and the CP in normal colon cells showed lower conformational dynamics compared with HCT116 CRC cells (Figure S10, Supporting Information). Notably, we were able to capture the individual FG-IDP conformational movements and interactions, which resembled CP formation states (Figure S4 and Video S3d, e, Supporting Information), which were overlooked in EM or cryo-EM studies. Surprisingly, we directly visualized inner lumen FG-NUPs from "transient mesh"-knots -CP phenotypes are reversible, which means that the CP or mesh-like central lumen can return to filaments, e.g. during cargo transportation. How to decide which states in the central lumen needs future investigation.

Long, flexible physical biofilaments are spontaneously tangled and knotted, from macroscopic fiber down to long-chain molecules [34]. Previous study has proposed an algorithm to determine a protein folding pathway that may explain how such a knot is formed [40,41]. Remarkably, our HS-AFM real-time imaging also showed FG filaments squirming and twisting during their interaction and the formation of transient knots that resemble CP (Fig. 1). Using HS-AFM, we captured the dynamics of a reversible conformational change in CP. The

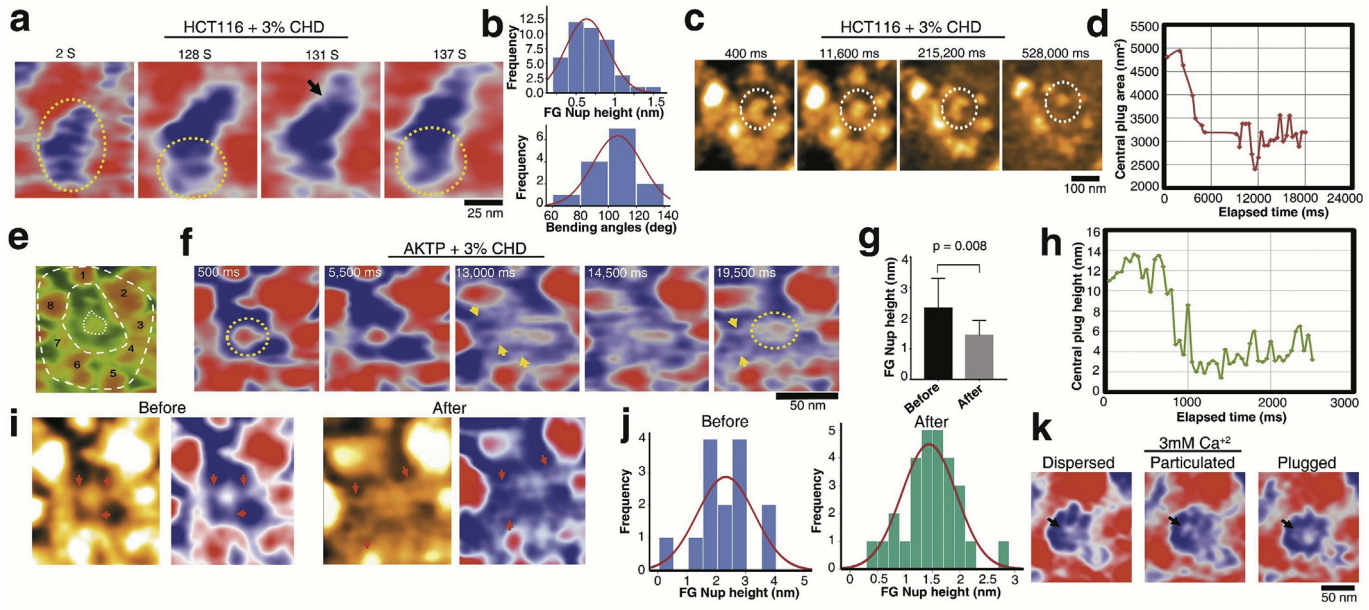

Fig. 7. Live tracking of central plug behavior in HCT116 cells and AKTP organoids treated with 1,2-hexanediol. (a) HS-AFM successive images of NPCs in HCT116 cells treated with 3% CHD. The FG-NUPs inside the central channel appear to be retracted to the edge in a time-dependent manner. The dotted circle shows the FG-NUP network tracking over time. The black arrows indicate some retracted FG-NUP filaments. Z-range is 8 nm, scanning speed is 1.7 frames per second, 200 × 200 pixels. **(b)** Normal distribution curve of FG-NUP heights (top) and FG-NUP filament bending angles (bottom) in CHD-treated HCT116 cells. **(c)** Successive HS-AFM images showing the effect of 3% CHD on the plugged NPC in HCT116 cells. Z-range is 12 nm, scanning speed is 2.5 frames per second, 200 × 200 pixels. **(d)** Surface area of central plug plotted against time. **(e)** HS-AFM image of a plugged NPC in AKTP organoids. Z-range is 25 nm, scanning speed is 2 frames per second, 200 × 200 pixels. **(f)** Successive HS-AFM images showing the effect of 3% CHD on the plugged NPC shown in **e**. The central plug degraded (yellow dotted circle) with elapsed time and single FG-NUP filaments (yellow arrows) started to appear after CP degradation. Z-range is 25 nm, scanning speed is 2 frames per second, 200 × 200 pixels. **(g)** Graph showing the difference in height of FG-NUPs before and after the destruction of CP. The FG-NUPs connected to the CP were measured. **(h)** Plot showing the reduction in height (thickness) of the central plug. **(i)** HS-AFM images showing the effect of 3% CHD on the plugged NPC before and after degradation of the central plug. Z-range is 25 nm, scanning speed is 2 frames per second, 200 × 200 pixels. **(j)** Normal distribution of FG-NUP heights before and after the degradation of the central plug in AKTP organoids. **(k)** High Ca^{+2} caused phase separation of FG-NUPs in HCT116 cells. Native NEs were treated with 3 mM Ca^{+2} which resulted in aggregation of the FG-NUP filaments to form different phases including dispersed, particulated and finally plugged phase which became a stable case under high Ca^{+2} levels (3 mM). Z-scale = 12 nm, speed = 2 frames/s, with 200 × 200 pixels. (For interpretation of the references to color in this figure legend, the reader is referred to the Web version of this article.)

morphology, identity and function of the CP/transporter have been long debated [1,4,7,10] Nevertheless, we provide the first direct observations and compelling evidence that FG-NUPs contribute to CP formation. CP ultra-fast conformational transitions were monitored in the nuclear inner central ring cells and organoids by HS-AFM (Fig. 7 and Video S5, S10, Supporting Information), hinting a straightforward correlation between CP components and IDP FG-NUPs. While further experiments and ideally more systems need to be identified and compared, our current data support the notion that the CP within the nuclear pore is at least partially composed of FG-IDPs (Fig. 8).

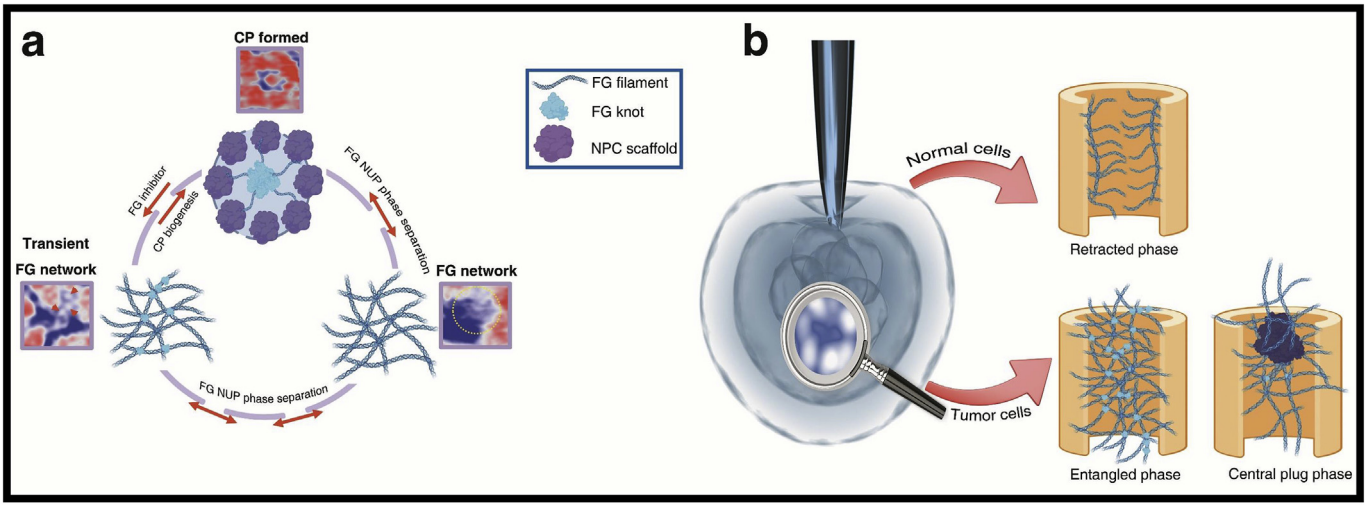

Fig. 8. HS-AFM as a powerful nano-diagnostic tool for tracing native single IDPs filaments. (a) Illustration showing different transient conformations of the FG-NUP network and the central plug, demonstrating how the CP is partially composed of FG-NUPs. **(b)** HS-AFM could be used to demonstrate the different nano-composition of single NPCs from different cell types, which can be used as an indication of the healthy or tumor state of cells based on the native NPC nano-structure.

Our work not only reveals that nano-biofilaments density are impending novel markers in cancers progression; but also implicates that isolated NE and NPCs are functional biocompatible and bio-recycled nanomaterials. Recent studies have shown that carbon nanotubes (CNT) or nano-channels can induce tumors and tumor-associated pathologies in lung cancer patients. From this view, another important insinuation of our work is that bio-recycled nanomaterials (BNM)-NPC nanopores have biocompatible advantages which directly derived from cells and organoids, rather than other engineered nanomaterials (ENM); opening a new avenue for nano-tissue engineering.

CRediT authorship contribution statement

Mahmoud Shaaban Mohamed: Investigation, Methodology, Formal analysis, Validation, Visualization, Data curation, Writing - review & editing. **Masaharu Hazawa:** Investigation, Validation, Visualization, Formal analysis. **Akiko Kobayashi:** Investigation, Formal analysis. **Laurent Guillaud:** Investigation, Formal analysis. **Takahiro Watanabe-Nakayama:** Methodology, Validation, Supervision. **Mizuho Nakayama:** Investigation, Resources. **Hanbo Wang:** Resources. **Noriyuki Kodera:** Resources, Validation, Supervision. **Masanobu Oshima:** Resources, Validation, Supervision. **Toshio Ando:** Resources, Validation, Supervision. **Richard W. Wong:** Conceptualization, Supervision, Project administration, Investigation, Funding acquisition, Visualization, Writing - original draft, Writing - review & editing.

Declaration of competing interest

The authors declare that they have no known competing financial interests or personal relationships that could have appeared to influence the work reported in this paper.

Acknowledgements

We also thank all members of the Wong laboratory. This work was supported by MEXT/JSPS KAKENHI grant numbers 17H05874 and 17K08655 (to R.W.) from MEXT Japan, and by grants from the Kobayashi International Scholarship Foundation (to R.W), and the Shimadzu Science Foundation (to R.W.).

Appendix A. Supplementary data

Supplementary data to this article can be found online at https://doi.org/10.1016/j.biomaterials.2020.120198.

References

[1] M. Beck, E. Hurt, Nat. Rev. Mol. Cell Biol. 18 (2017) 73.
[2] A. Hoelz, G. Blobel, Nature 432 (2004) 815.
[3] K.E. Knockenhauer, T.U. Schwartz, Cell 164 (2016) 1162.
[4] K.S. Lim, R.W. Wong, Cell Chem. Biol. 25 (2018) 1056.
[5] G. Celetti, G. Paci, J. Caria, V. VanDelinder, G. Bachand, E.A. Lemke, J. Cell Biol. 219 (2020) e201907157.
[6] G.J. Stanley, A. Fassati, B.W. Hoogenboom, Semin. Cell Dev. Biol. 68 (2017) 42.
[7] C.W. Akey, J. Mol. Biol. 248 (1995) 273.
[8] C.W. Akey, Structure 18 (2010) 1230.
[9] S.J. Kim, J. Fernandez-Martinez, I. Nudelman, Y. Shi, W. Zhang, B. Raveh, T. Herricks, B.D. Slaughter, J.A. Hogan, P. Upla, I.E. Chemmama, R. Pellarin, I. Echeverria, M. Shivaraju, A.S. Chaudhury, J. Wang, R. Williams, J.R. Unruh, C.H. Greenberg, E.Y. Jacobs, Z. Yu, M.J. de la Cruz, R. Mironska, D.L. Stokes, J.D. Aitchison, M.F. Jarrold, J.L. Gerton, S.J. Ludtke, C.W. Akey, B.T. Chait, A. Sali, M.P. Rout, Nature 555 (2018) 475.
[10] V. Shahin, Semin. *Cell Dev. Biol.* 68 (2017) 85.
[11] C. Leung, A.W. Hodel, A.J. Brennan, N. Lukoyanova, S. Tran, C.M. House, S.C. Kondos, J.C. Whisstock, M.A. Dunstone, J.A. Trapani, I. Voskoboinik, H.R. Saibil, B.W. Hoogenboom, Nat. Nanotechnol. 12 (2017) 467.
[12] R. Gao, S.M. Asano, S. Upadhyayula, I. Pisarev, D.E. Milkie, T.L. Liu, V. Singh, A. Graves, G.H. Huynh, Y. Zhao, J. Bogovic, J. Colonell, C.M. Ott, C. Zugates, S. Tappan, A. Rodriguez, K.R. Mosaliganti, S.H. Sheu, H.A. Pasolli, S. Pang, C.S. Xu, S.G. Megason, H. Hess, J. Lippincott-Schwartz, A. Hantman, G.M. Rubin, T. Kirchhausen, S. Saalfeld, Y. Aso, E.S. Boyden, E. Betzig, Science (2019) 363.
[13] T. Ando, N. Kodera, Methods Mol. Biol. 896 (2012) 57.
[14] T. Ando, Biophys. Rev. 10 (2018) 285.
[15] T. Uchihashi, S. Scheuring, Biochim. Biophys. Acta Gen. Subj. 1862 (2018) 229.
[16] Y. Sakiyama, A. Mazur, L.E. Kapinos, R.Y.H. Lim, Nat. Nanotechnol. 11 (2016) 719.
[17] M.S. Mohamed, A. Kobayashi, A. Taoka, T. Watanabe-Nakayama, Y. Kikuchi, M. Hazawa, T. Minamoto, Y. Fukumori, N. Kodera, T. Uchihashi, T. Ando, R.W. Wong, ACS Nano 11 (2017) 5567.
[18] E. Sakai, M. Nakayama, H. Oshima, Y. Kouyama, A. Niida, S. Fujii, A. Ochiai, K.I. Nakayama, K. Mimori, Y. Suzuki, C.P. Hong, C.Y. Ock, S.J. Kim, M. Oshima, Canc. Res. 78 (2018) 1334.
[19] S. Krull, J. Thyberg, B. Bjorkroth, H.R. Rackwitz, V.C. Cordes, Mol. Biol. Cell 15 (2004) 4261.
[20] A.R. Lowe, J.H. Tang, J. Yassif, M. Graf, W.Y. Huang, J.T. Groves, K. Weis, J.T. Liphardt, Elife 4 (2015).
[21] N.B. Eisele, A.A. Labokha, S. Frey, D. Gorlich, R.P. Richter, Biophys. J. 105 (2013) 1860.
[22] R. Peters, Traffic 6 (2005) 421.
[23] K.Y. Shi, E. Mori, Z.F. Nizami, Y. Lin, M. Kato, S. Xiang, L.C. Wu, M. Ding, Y. Yu, J.G. Gall, S.L. McKnight, Proc. Natl. Acad. Sci. U. S. A. 114 (2017) E1111.
[24] D. Stoffler, K.N. Goldie, B. Feja, U. Aebi, J. Mol. Biol. 287 (1999) 741.
[25] M. Eibauer, M. Pellanda, Y. Turgay, A. Dubrovsky, A. Wild, O. Medalia, Nat. Commun. 6 (2015) 7532.
[26] H.W. Shin, H. Choi, D. So, Y.I. Kim, K. Cho, H.J. Chung, K.H. Lee, Y.S. Chun, C.H. Cho, G.H. Kang, W.H. Kim, J.W. Park, Gastroenterology 147 (2014) 430.
[27] F. Takahashi-Yanaga, T. Yoshihara, K. Jingushi, K. Igawa, K. Tomooka, Y. Watanabe, S. Morimoto, Y. Nakatsu, T. Tsuzuki, Y. Nakabeppu, T. Sasaguri, Biochem. Pharmacol. 89 (2014) 340.
[28] M. Nakayama, E. Sakai, K. Echizen, Y. Yamada, H. Oshima, T.S. Han, R. Ohki, S. Fujii, A. Ochiai, S. Robine, D.C. Voon, T. Tanaka, M.M. Taketo, M. Oshima, Oncogene 36 (2017) 5885.
[29] I. Liashkovich, D. Pasrednik, V. Prystopiuk, G. Rosso, H. Oberleithner, V. Shahin, Sci. Rep. 5 (2015) 9994.
[30] E. Onischenko, J.H. Tang, K.R. Andersen, K.E. Knockenhauer, P. Vallotton, C.P. Derrer, A. Kralt, C.F. Mugler, L.Y. Chan, T.U. Schwartz, K. Weis, Cell 171 (2017) 904.
[31] Y.M. Chook, G. Blobel, Nature 399 (1999) 230.
[32] T. Odijk, Phys. Rev. E - Stat. Nonlinear Soft Matter Phys. 77 (2008) 060901.
[33] E. Terriac, S. Schutz, F. Lautenschlager, Front. Cell Dev. Biol. 7 (2019) 106.
[34] K. Alexander, A.J. Taylor, M.R. Dennis, Sci. Rep. 7 (2017) 42300.
[35] T.B. Liverpool, A.C. Maggs, Macromolecules 34 (2001) 6064.
[36] M. Doi, S.F. Edwards, Oxford University Press, New York, 1986.
[37] T.T. Perkins, D.E. Smith, S. Chu, Science 264 (1994) 819.
[38] J. Kas, H. Strey, E. Sackmann, Nature 368 (1994) 226.
[39] M. Keshavarz, H. Engelkamp, J. Xu, E. Braeken, M.B. Otten, I.H. Uji, E. Schwartz, M. Koepf, A. Vananroye, J. Vermant, R.J. Nolte, F. De Schryver, J.C. Maan, J. Hofkens, P.C. Christianen, A.E. Rowan, ACS Nano 10 (2016) 1434.
[40] V. Shahin, I.U. Kouzel, G. Rosso, I. Liashkovich, Adv. Sci. 6 (2019) 1900709.
[41] W.R. Taylor, Nature 406 (2000) 916.
[42] A.L. Mallam, S.E. Jackson, Nat. Chem. Biol. 8 (2012) 147.
[43] N. Tarantino, J.Y. Tinevez, E.F. Crowell, B. Boisson, R. Henriques, M. Mhlanga, F. Agou, A. Israel, E. Laplantine, J. Cell Biol. 204 (2014) 231.
[44] M. Hazawa, D.C. Lin, A. Kobayashi, Y.Y. Jiang, L. Xu, F.R.P. Dewi, M.S. Mohamed, Hartono, M. Nakada, M. Meguro-Horike, S.I. Horike, H.P. Koeffler, R.W. Wong, EMBO Rep. 19 (2018) 73.
[45] F.R.P. Dewi, S. Jiapaer, A. Kobayashi, M. Hazawa, D.K. Ikliptikawati, Hartono, H. Sabit, M. Nakada, R.W. Wong, Autophagy 24 (2020) 1.
[46] M. Hazawa, D.C. Lin, H. Handral, L. Xu, Y. Chen, Y.Y. Jiang, A. Mayakonda, L.W. Ding, X. Meng, A. Sharma, S. Samuel, M.M. Movahednia, R.W. Wong, H. Yang, C. Tong, H.P. Koeffler, Oncogene 36 (2017) 2243.
[47] B. Hampoelz, A. Andres-Pons, P. Kastritis, M. Beck, Annu. Rev. Biophys. 48 (2019) 515.
[48] K.M. Reid, P. Sunanda, S. Raghothama, V.V. Krishnan, Biopolymers 108 (6) (2017 Nov).
[49] G.J. Stanley, B. Akpinar, Q. Shen, P.D.E. Fisher, C.P. Lusk, C. Lin, B.W. Hoogenboom, ACS Nano 13 (7) (2019 Jul 23) 7949–7956.
[50] Martin Beck, Friedrich Förster, Mary Ecke, Jürgen M. Plitzko, Frauke Melchior, Günther Gerisch, Wolfgang Baumeister, Ohad medalia, Science 306 (2004) 1387.
[51] S.S.1 Patel, B.J. Belmont, J.M. Sante, M.F. Rexach, Cell 6 (1) (2007) 129.
[52] K.1 Ribbeck, D. Görlich, EMBO J. 3 (11) (2002) 21.